Stereophotoclinometry on the OSIRIS-REx Mission: Mathematics and Methods

R.W. Gaskell[1], O.S.Barnouin[2], M.G. Daly[3], E.E. Palmer[1], J.R. Weirich[1], C. M. Ernst[2], R.T. Daly[2], D.S. Lauretta[4]

[1]Planetary Science Institute, Tucson, AZ, 85719, USA
[2]The Johns Hopkins University Applied Physics Laboratory, Laurel, MD, USA
[3]The Centre for Research in Earth and Space Science, York University, Toronto, ON, Canada
[4]Lunar and Planetary Laboratory, University of Arizona, Tucson, AZ, USA

ABSTRACT

Stereophotoclinometry (SPC) makes it possible to extract the shape of surfaces by combining information from images, namely stereo parallax data and surface shading from slopes, with knowledge of the location of a spacecraft. This technique has been used extensively in the past few decades to describe the shape of planets and small bodies, such as asteroids and comets. It has also been used to navigate spacecraft carefully around very small bodies, as in the case of the OSIRIS-REx mission to the ~500-m-diameter asteroid (101955) Bennu. This paper describes the mathematical foundation of SPC, with examples from the OSIRIS-REx mission.

1. Introduction

Stereophotoclinometry (SPC; licensible from the Planetary Science Institute - see acknowledgement) uses images to estimate stereo parallax and surface shading from slopes along with knowledge of the spacecraft location to compute topography. SPC has been an evolving tool for navigation and shape modeling for the past three decades. The current and past implementations of SPC have been successfully used to model the shapes of many small bodies, satellites, and planets, including but not limited to Vesta (Gaskell, 2012), Ceres (Park and Buccino, 2018), Eros (Gaskell, 2008), Itokawa (Gaskell et al., 2006, 2008), Mathilde (Weirich et al., 2019), Bennu (Barnouin et al., 2019, Palmer et al., 2022), Ryugu (Watanabe et al., 2019), 67P/Churyumov–Gerasimenko (Gaskell et al. 2014, Jorda et al. 2016), 9P/Tempel 1 (Ernst et al. 2019), the Moon (Gaskell et al. 2011, Weirich et al. 2019), Phobos and Deimos (Gaskell, 2020; Ernst et al., 2022), Io (Gaskell et al., 1988), Janus (Daly et al., 2018), Phoebe (Gaskell, 2013), and Mercury (Perry et al., 2015). The software can also be licensed for use in other projects as described in the Acknowledgements.

The basic idea behind SPC is to use landmarks, which are the centers of small local maps of a body's surface, called “maplets”, as control points for navigation and cartography. Maplets contain both topographic and albedo information. Each maplet is associated with multiple images. The three-dimensional location of the center of each maplet is estimated from stereo parallax provided by the multiple contributing images.

This location places the maplet in a body-fixed frame relative to the center of the object being modeled. With this stereo result, each maplet is illuminated to match the geometry of each one of the associated images that are used to model the maplet. A maplet's pixel/line location in a given image is determined by correlating the brightness variations across the illuminated maplet with the orthorectified image. The illumination of a maplet itself depends on the local incidence and emission angles, phase angle, and local albedo. By comparing the maplet brightness with the image brightness for many images, the maplet's slope and albedo distribution can be determined, and the slope distribution can then be integrated to determine the topography.

If a single maplet can be found in many images and the spacecraft state when each image was acquired is known, then the location of the maplet on the body's surface can be determined by combining the stereo information and the surface brightness variations. If a single image can be found in many maplets and these maplets' locations on the body's surface are known, then the spacecraft (s/c) state (i.e., position and orientation) at the time of the image can be determined. SPC iterates through solutions for spacecraft state and maplet position to arrive at a self-consistent solution for both. A simultaneous solution for s/c state and maplet position (bundle adjustment) is usually impossible owing to the tens to hundreds of thousands of images and maplets commonly used. Instead SPC solves for (i) maplet surface shape, (ii) landmarks (maplet center), and (iii) the s/c state in three separate loops (Figure 1). The first loop uses images to improve maplet surface models and provides initial estimates of a maplet center, while the second updates the landmarks further by adjusting the landmark vectors. Both can be run in a parallel process mode. The third loop is done occasionally because of a slightly better knowledge of the s/c state and the locations of the maplets themselves from the other just mentioned iterations. It is usually undertaken as new images are added to the SPC process, during the course of a mission.

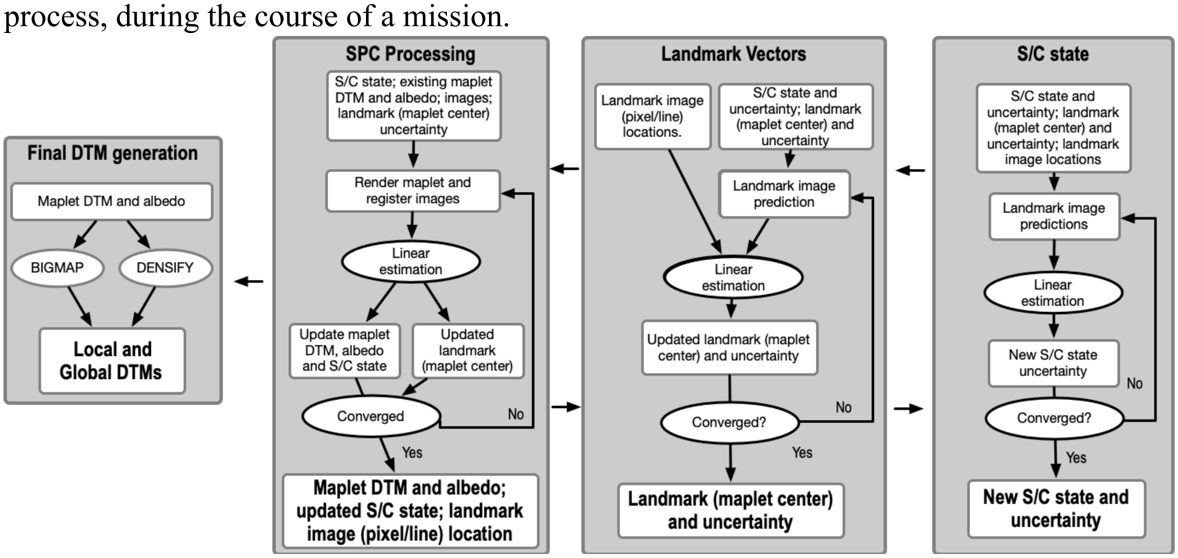

Figure 1. The three main loops of SPC (right) with inputs (left) for generating the final set of digital terrain models (DTMs). Convergence of the S/C position and attitude, and the regional DTM's surface and center, end the SPC estimation process (Palmer et al. 2022).

A large number of overlapping maplets can be combined to produce a global topography model. Image data alone cannot independently solve for the size of the object and the spacecraft distance. SPC requires additional information to get around this size/distance degeneracy. For large bodies, accurate navigation is possible using radio science measurements alone owing to the large gravitational parameter (*GM*) that produces an easily detectable Doppler signal. For small bodies, imaging combined with Doppler-determined approach velocity can provide an accurate range and therefore size estimate. If laser ranging is available, then a combination of SPC navigation and shape with an absolute knowledge of the distance to the surface can provide precise estimates of the spacecraft position and the body's size.

This paper lays out the mathematics of SPC, as applied to in-flight shape modeling and navigation. The examples provided are from the OSIRIS-REx (Origins, Spectral Interpretation, Resource Identification, and Security–Regolith Explorer) mission to the ~500-m-diameter asteroid (101955) Bennu (e.g., Lauretta et al., 2017, 2019, 2021). Section 2 discusses the input data needed to begin the SPC process. Section 3 delves into the mathematics behind the linear estimation technique used throughout SPC. Section 4 details how to build successively higher-resolution maplets. Section 5 discusses how to use a set of maplets to build both regional and global DTMs). Section 6 demonstrates how altimetry data can be used to improve the SPC solution. Section 7 summarizes the SPC software implementation.

This paper emphasizes the mathematics behind SPC and how altimetric data can be included in SPC solutions. Three companion papers (Palmer et al., 2022, Mario et al., 2022, Adam et al., 2022) provide details on implementing SPC to model the surface of Bennu (and other asteroids) and navigate a spacecraft. The accuracy of SPC is further discussed in Al Asad et al. (2021) for results obtained during the OSIRIS-REx mission at Bennu and Weirich et al. (2022) for pre-flight testing with a synthetic asteroid. Daly et al. (2022) discuss the expected SPC performance during a flyby and impact mission. Reviews of SPC's uncertainties are also described in Barnouin et al. (2020).

2. Inputs

SPC requires several inputs. The following sub-sections discuss the images, camera models, the Navigation and Ancillary Information Facility's (NAIF's) Spacecraft, Planet, Instrument, Camera-matrix and Event (SPICE) information, and a starting shape model.

2.1. Images

A major advantage of SPC is that it can incorporate nearly any type of image and imaging geometry and will provide a fairly quick initial solution for the shape of an object. Original images in any format — PDS IMG and Flexible Image Transport System (FITS) files are the most common — are processed to produce the raw 8- or 16-bit format used by SPC. While calibrated images can be used, some basic calibration of raw images is possible within the SPC framework, including flat fielding and removal of dark current and frame transfer smear. Usually, a pre-processing program for each individual camera is required, owing to differences in the properties of the camera and its calibration, as well as image header practices. Although unsigned short, most significant bit (MSB) images are preferred, SPC can recognize and distinguish between other 16-bit formats. Image names are restricted to 12 characters, so it is often necessary to rename the images. A commonly used name consists of a one-character camera identifier, nine characters for the integral part of the ephemeris time, and two characters identifying the filter(s), if any.

The fidelity of the solution improves with additional processing and optimal imaging. The best solutions are obtained when at least five images are available in suitable geometries and lighting conditions (see Barnouin et al. 2020 and Palmer et al. 2022 for more details) to take full advantage of both stereo and photoclinometry. Nevertheless, SPC remains a highly capable software able to produce good solutions even with very limited data (Daly et al., 2022).

For OSIRIS-REx, the imaging for SPC was primarily performed using the PolyCam narrow-field and MapCam medium-field imagers of the OSIRIS-REx Camera Suite (OCAMS; Rizk et al., 2018; Golish et al., 2020), as well as NavCam 1 imager of the Touch and Go Camera System (TAGCAMS; Bos et al., 2018, 2020). During rehearsals and execution of sample collection (Lauretta et al., 2021, 2022; Wibben et al., 2022), SamCam (OCAMS) and NavCam 2 (TAGCAMS) images were used, allowing a precise SPC reconstruction of the spacecraft's trajectory during these operations.

2.2. Camera models (+ distortion)

SPC requires a camera model to translate the image data from pixel space on the detector into physical space. A camera model must capture the detector dimensions, the shapes and sizes of the pixels, the central pixel/line (also referred to as sample/line) of the optical axis, the focal length of the camera, and a distortion model. The following is specific to framing cameras. SPC has also been used with line-scan data, but the treatment is slightly different (see Section 8 for additional details).

The first approximation to a camera model is a gnomonic projection or pinhole camera. If $\mathbf{C}_x$, $\mathbf{C}_y$, and $\mathbf{C}_z$ are the unit vectors of the camera frame, with $\mathbf{C}_z$ in the boresight direction, then if $\mathbf{W}$ is a vector from the pinhole to a point in space, the projection of that point onto the focal plane has the coordinates

$$x_p = f\frac{W\cdot\mathbf{C_x}}{W\cdot\mathbf{C_z}} \qquad y_p = f\frac{W\cdot\mathbf{C_y}}{W\cdot\mathbf{C_z}} \qquad (1)$$

where f is the focal length, the distance from the pinhole to the focal plane. Lenses and mirrors are not pinholes, of course. There are always distortions, and the true focal plane position is

$$x = x_p + dx(x_p, y_p) \qquad y = y_p + dy(x_p, y_p) \qquad (2)$$

The actual location in an image, measured as a pixel/line pair starting from 1,1 in the upper left corner, is

$$p = p_0 + K_{xx}x + K_{xy}y \qquad l = l_0 + K_{yx}x + K_{yy}y \qquad (3)$$

The distortion parameters in dx and dy, the central pixel p_0, l_0, the focal length, and the K-matrix are determined by minimizing the summed squared residuals between the observed image space positions of stars in many images taken during cruise and the predicted positions based on the nominal parameters and the locations of the stars in a catalog, such as Tycho 2 (available from NAIF, 2007). Also determined is the camera orientation relative to the spacecraft frame. K_{xx} is not solved for but is the inverse of the measured linear pixel size and has units of pixels per millimeter. If there is an extra reflection when an odd number of mirrors is present in the camera optics, the sign change occurs in K_{yy} (Owen, 2011). While the model used by Owen (2011) is the most commonly employed in our implementation of SPC, several additional distortion models are available, and it is easy to add more. Currently, SPC supports an Open CV model for OSIRIS-REx, a form for the Hasselblad camera for the Apollo lunar data, a general USGS model, mission-specific forms from ROSETTA and Hayabusa2, a bi-cubic model, and a model for line-scan cameras.

A change in temperature is likely to expand or contract the optical path in the camera, leading to a temperature variation in the focal length that can be determined with enough star observations (e.g., for the NEAR [Near Earth Asteroid Rendezvous] spacecraft; Murchie et al. 2002). A file containing linear temperature variations for each camera can now be read by the core program LITHOS of the SPC software package developed by Gaskell et al. (2008).

2.3. SPICE info

SPC operates in a body-fixed coordinate system and uses SPICE information (Acton 1996; Acton et al. 2018) to relate the inertial, spacecraft and camera frames to the body-fixed frame. SPC requires a planetary constants kernel (pck, contains information about the body rotation rate, rotation axis, and prime meridian), leapsecond kernel (lsk), spacecraft clock kernel (sclk), spacecraft ephemeris kernel (spk), spacecraft attitude kernel (ck), instrument kernel (ik), and a frames kernel fk). A SPICE kernel is a data file that contains detailed spacecraft navigation and physical model parameter values needed to compute the camera viewing geometry for each observation. A detailed description of how SPC uses SPICE information can be found in Palmer et al. (2022). Along with information extracted from the headers of the original images, these data provide initial or nominal solutions for the S/C location and attitude; SPC updates these as processing of the images is undertaken and a surface model is built.

Used for the first time on OSIRIS-REx, the SPC software can also account for the displacement between the spacecraft center of mass (which is used to determine a spacecraft trajectory in the SPICE spks) and the pupil (pinhole) for each camera. This shift is not negligible for large spacecraft that may need to interact with a surface, to ensure DTM and navigation solutions at the centimeter level.

Information about the camera (Section 2.1) and the spacecraft state at the time of imaging are derived from the original image header data within the SPICE kernels. These data are kept in a separate summary file for each image called <image name>.SUM. This file also contains thresholds: a lower one below which data are assumed to be in shadow or not on the body, and an upper one usually representing the upper end of the data (255 for 8-bit, 4095 for 12-bit, etc.). In some cases, the upper threshold is set smaller to filter out bright backgrounds, such as Mars in the case of Phobos observations. In other cases, when a camera has sufficient dynamic range to show regions of secondary illumination in shadowed areas, the lower threshold must be raised. We have developed special procedures to extract SPC data from this secondary illumination.

2.4. Starting model

SPC requires a starting shape model to provide the curvature and initial topography estimation for the initial set of large maplets. For large bodies like planets or large satellites, the initial shape is typically a tri-axial ellipsoid whose axes are well known. For smaller bodies, there may be radar models or perhaps only lightcurve analyses. In the latter cases, the starting shape model must be built on the fly during approach. Limbs identified in approach images provide a valuable source of information for creating a starter model (see Section 3.2 for details of how SPC finds and incorporates limbs).

A limb-based model made from approach images was used as a starting shape for OSIRIS-REx. During OSIRIS-REx's approach to Bennu, the asteroid appeared at very low phase angle. Limbs were exploited to build an initial shape model (Figure 2). This initial shape model was used to register (align) the images. Predicted and observed limb positions in the image were used to correct the surface vectors. The resulting cloud of vectors, along with a subset of vectors from the original shape, were fit with a spherical harmonic expansion of degree and order 15 to create a new shape model. This procedure was iterated until it converged. See Palmer et al. (2022) for more details on starter models for general cases and OSIRIS-REx specifically.

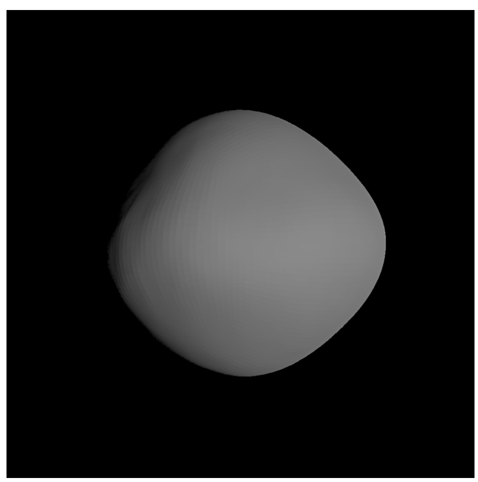

Figure 2. Initial Bennu shape model constructed from approach limb data.

3. The mathematical foundation: linear estimation

The current SPC implementation makes extensive use of linear estimation to determine various quantities, including spacecraft position, camera pointing, surface locations, surface tilts, and surface albedo from observables, such as camera pixel location and measured surface brightness. The assumption behind linear estimation is that, from a starting point close enough to the solution, there is a linear relationship between observable and the quantity of interest. As is commonplace in such estimation, the SPC presented here handles noise and biases. In the following section, we use variable **q** to represent either s/c position or camera pointing, but it can represent any quantity that affects the prediction *P*. Also, as stated earlier (Section 1), the SPC implementation discussed here solves for s/c state in one loop, landmark (maplet center) in another loop (section 3.1), and local maplet DTMs in a third (Section 3.3). It does not solve for all these variables simultaneously; rather, SPC iterates between the three until residual differences converge.

3.1. *Estimating a spacecraft's position and camera pointing geometry*

Here, we focus on the estimation of geometric parameters associated with spacecraft location and camera pointing. A key aspect of SPC is that we solve for several different quantities of $\mathbf{q}$ (s/c state, maplet center, and maplet dtm and albedo) by treating each separately, and using formal uncertainties of one quantity in the weighting of the other. By separating out the solution between a few quantities, we can break a big problem into many smaller ones.

The quantity q_i (spacecraft x-, y- and z-vector components, for example) are approximately known using a priori SPICE data (Section 2.3). Their nominal values are used to compute the difference between a predicted value $P(\mathbf{q})$ (the predicted location of a landmark in a given image for a vector $\mathbf{q}$, for example) and an observable O (the observed location of the landmark in an image). The q_i are varied by amounts δq_i to minimize the summed square residuals

$$\sum \frac{\left(O-P(\mathbf{q}+\delta\mathbf{q})\right)^2}{\sigma^2} \approx \sum \frac{\left(O-P(\mathbf{q})-\delta q_i \frac{\partial P}{\partial q_i}\right)^2}{\sigma^2} \quad (4)$$

where σ is the uncertainty of each measurement and repeated indices are summed. The sigmas (σ) in this equation and those below are purely schematic. They are stand-ins for a set of weights that may have different values, appropriate to each term in the summation. Initial weights are determined from known uncertainties in the s/c state, and camera properties. Altimetric data, if available, can also contribute to the determination of the initial weights. As the estimation proceeds, the weights are equated to the diagonals of the covariance matrix of the s/c state or landmark estimation (or formal uncertainties). The sum in eq. 4 is over all the observations, so, when solving for spacecraft position, the sum is over all the landmarks in a given image from which the position is solved. The minimum is found by setting the derivatives of eq. 4 with respect to δq_i to zero to obtain

$$\sum \frac{\frac{\partial P}{\partial q_i}\left(O-P(\mathbf{q})-\delta q_j \frac{\partial P}{\partial q_j}\right)}{\sigma^2} = 0 \qquad (5)$$

$$\sum \frac{\frac{\partial P}{\partial q_i}\left(O-P(\mathbf{q})\right)}{\sigma^2} = \left[\sum \frac{\frac{\partial P}{\partial q_i}\frac{\partial P}{\partial q_j}}{\sigma^2}\right] \delta q_j \quad (6)$$

The bracketed term on the right side is a symmetric information matrix M_{ij}, and the left side is called w_i. Multiplying both sides of eq. 6 by the covariance matrix $M^{-1}{}_{ki}$ provides the estimate for the changes to q:

$$\delta q_k = M^{-1}{}_{ki} w_i \qquad (7)$$

Constraint terms are frequently included in eq. 4 of the form $(Q - q_i - \delta q_i)^2/\sigma^2$, resulting in additions $(Q - q_i)/\sigma^2$ to w_i and $1/\sigma^2$ to the diagonal elements M_{ii}. These are typically included to encourage, for example, the spacecraft position to not wander too far from the navigation solution or the pointing to remain close to the star tracker determination. This is especially important for a narrow-angle camera where there is a correlation between cross boresight pointing and spacecraft position. Two other constraints reduce noise by tying together neighboring solutions. Nearby spacecraft position solutions are tied to each other using the trajectory solution provided by the Flight Dynamics team, while solutions for central vectors of overlapping maplets are tied together by correlating the common topography in the overlap regions.

SPC locates common control points on a body's surface in images. Observations of a single control point in many images allows its position on the surface to be determined. Observations of many control points in a single image allows the spacecraft state (position and orientation) at the imaging time to be found. The vector **W** from the spacecraft (actually the pupil) to a surface point is the sum of the spacecraft-object vector $\mathbf{V_0}$ and the surface position vector **V**. All these vectors are defined in the body-fixed reference frame of the target (Figure 3). If the camera orientation is also known, then the image space location of the surface point (p_p, l_p) can be predicted with eqs. 1–3. The summed squared residuals to be minimized are now $\Sigma\ [(p_o - p_p)^2/\sigma^2 + (l_o - l_p)^2/\sigma^2]$. The sum Σ is over all images if a maplet vector **V** is being determined or over all maplets if a spacecraft state is being estimated. A small change $\delta\mathbf{W}$ in either **V** or $\mathbf{V}_0$ leads to the changes $\delta p = \Sigma \delta W_i \partial p / \partial W_i$ and $\delta l = \Sigma \delta W_i \partial l / \partial W_i$, where the partials are

$$\begin{aligned} \frac{\partial p}{\partial W_i} &= f K_{xx} \frac{C_{xi} W \cdot \mathbf{C_z} - C_{zi} W \cdot \mathbf{C_x}}{(W \cdot \mathbf{C_z})^2} \\ \frac{\partial l}{\partial W_i} &= f K_{yy} \frac{C_{yi} W \cdot \mathbf{C_z} - C_{zi} W \cdot \mathbf{C_y}}{(W \cdot \mathbf{C_z})^2} \end{aligned} \qquad (8)$$

The distortion terms in eq. 2 and the off-diagonal *K*-matrix elements in eq. 3 are ignored because the solution converges rapidly to the same solution without them.

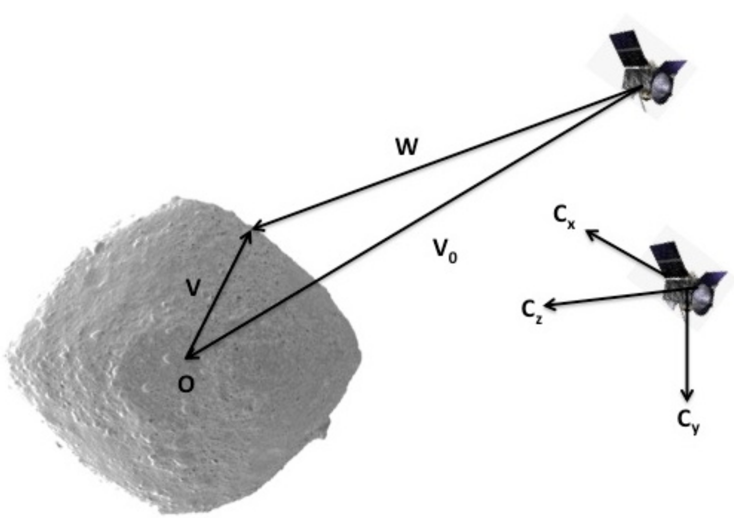

Figure 3. Definition of spacecraft-object ($\mathbf{V}_0$), maplet ($\mathbf{V}$), and camera orientation ($\mathbf{C_x}$, $\mathbf{C_y}$ and $\mathbf{C_z}$) vectors. **W** is the spacecraft-surface vector and **O** is the origin of the body-fixed reference frame.

A new maplet vector $\mathbf{V}'$ with fixed spacecraft state is then determined by using:

$$M_{ij} = \Sigma[(\partial p/\partial W_i \partial p/\partial W_j)/\sigma^2 + (\partial l/\partial W_i \partial l/\partial W_j)/\sigma^2] \qquad (i,j=1,3) \qquad (9)$$
$$w_i = \Sigma[((p_o - p_p)\partial p/\partial W_i)/\sigma^2 + ((l_o - l_p)\partial l/\partial W_i)/\sigma^2]$$

and the sum is over all the images used. Recall that $\mathbf{W}=\mathbf{V}+\mathbf{V}_0$. The components of the maplet vector $\mathbf{V}'$ then become

$$V'_i = V_i + M^{-1}_{ik} w_k \pm \sqrt{M^{-1}_{ii}} \qquad (i,k=1,3) \qquad (10)$$

The last term is the formal uncertainty. It feeds into the determination of the sigmas for the spacecraft state estimation. The inverse of the symmetric matrix **M** is accomplished by first using a Cholesky decomposition to write $\mathbf{M} = \mathbf{U}^\mathbf{T}\mathbf{D}\mathbf{U}$, where **U** is upper triangular with unit diagonal elements and **D** is diagonal. **U** and (trivially) **D** are then inverted to form the inverse. The matrices solved here are neither large nor sparse because we alternate between s/c state (6x6) and landmark vector **V** (3x3) solutions, with formal uncertainties of one participating in the weighting of the other.

To solve for $\mathbf{V}_0$, we also need to estimate the camera orientation. We perform this estimate for small rotations (τ_1, τ_2, τ_3) about the orthonormal camera vectors $\mathbf{C_x}$, $\mathbf{C_y}$, and $\mathbf{C_z}$ respectively. The linearized changes in these vectors are

$$\delta\mathbf{C_x} = \tau_3\mathbf{C_y} - \tau_2\mathbf{C_z}\,,\ \delta\mathbf{C_y} = \tau_1\mathbf{C_z} - \tau_3\mathbf{C_x}\,,\ \delta\mathbf{C_z} = \tau_2\mathbf{C_x} - \tau_1\mathbf{C_y} \qquad (11)$$

and the resulting partials are

$$\partial p/\partial \tau_1 \approx fK_{xx}(\mathbf{W}\bullet\mathbf{C}_x)(\mathbf{W}\bullet\mathbf{C_y})/(\mathbf{W}\bullet\mathbf{C_z})^2 \quad \partial l/\partial \tau_1 \approx fK_{yy}(1+(\mathbf{W}\bullet\mathbf{C_y})^2/(\mathbf{W}\bullet\mathbf{C_z})^2)$$

$$\partial p/\partial \tau_2 \approx -fK_{xx}(1+(\mathbf{W}\bullet\mathbf{C}_x)^2/(\mathbf{W}\bullet\mathbf{C_z})^2) \quad \partial l/\partial \tau_2 \approx -fK_{yy}(\mathbf{W}\bullet\mathbf{C_x})(\mathbf{W}\bullet\mathbf{C_y})/(\mathbf{W}\bullet\mathbf{C_z})^2$$

$$\partial p/\partial \tau_3 \approx fK_{xx}(\mathbf{W}\bullet\mathbf{C_y})/(\mathbf{W}\bullet\mathbf{C_z}) \qquad \partial \mathrm{l}/\partial \tau_3 \approx -fK_{yy}(\mathbf{W}\bullet\mathbf{C_x})/(\mathbf{W}\bullet\mathbf{C_z}) \qquad (12)$$

To facilitate the spacecraft state estimation, δV_{0i} is written as τ_{i+3} so $\partial/\partial V_{0i} = \partial/\partial W_i = \partial/\partial\ \tau_{i+3}$ and

$$M_{ij} = \Sigma[(\partial p/\partial \tau_i \partial p/\partial \tau_j)\ /\sigma^2 + (\partial l/\partial \tau_i \partial l/\partial \tau_j)\ /\sigma^2] \qquad (i,j=1,6) \quad (13)$$
$$w_i = \Sigma[((p_o - p_p)\partial p/\partial \tau_i)/\sigma^2 + ((l_o - l_p)\partial l/\partial \tau_i)/\sigma^2]$$

where the partials for p and l are defined in eqs. 8 and 12, and the sum is over all the maplets in an image. The new estimate for the spacecraft-object vector $\mathbf{V}'_0$ then becomes

$$V'_{0i} = V_{0i} + \tau_{i+3} = V_{0i} + M^{-1}_{i+3,k} w_k \pm \sqrt{M^{-1}_{i+3,i+3}} \quad (i=1,3,\ k=1,6) \quad (14)$$

The rotation parameters $\tau_i = M^{-1}_{i,k} w_k$ (i=1,3, k=1,6) are used with eq. 11 to update $\mathbf{C_x}$, $\mathbf{C_y}$, and $\mathbf{C_z}$, but because this is just a linear approximation, it is necessary to ortho-normalize these vectors at the end. This estimation is performed separately over each image.

The final root-mean-square (RMS) residuals $<(O–P)^2>$ provide a goodness of fit (GOF) for each maplet and for each image that can be used to identify problem areas. For the overall fit, which includes all maplets and images, $O–P$ is projected and scaled from the native pixel/line observables to a common linear scale, with the linear RMS residual giving a GOF for the entire solution. The transformation between inertial space — where the orientation of the camera (relative to the fixed stars) and the spacecraft position are determined — and the body-fixed frame in which SPC functions is set by the inertial space orientation of the body's pole and its rotational period. Initially, these are determined during approach or even by lightcurve or radar analysis years in advance, and are taken as fixed during the solution process. As processing continues, it may become apparent that the pole is not quite right. An efficient approach for finding a new pole is to converge complete solutions for many pole choices in order to find the smallest linear RMS residual. In practice, a reduced set of maplets and images is used to speed up the processing.

3.2. Identifying limbs

Predicted limb positions in a given image are those points V_L on the shape model for which a line of sight is tangent to the surface. The vector from the spacecraft to this point is $W=V_0+ V_L$, and its position in image space is determined from eqs. 1–3. The limb scan to determine the actual V_L begins at some distance above the surface at $V_L + \kappa N$, where N is the normal to the surface and where the corresponding image brightness is below a threshold for illumination. As κ is decreased, the observed brightness finally starts to increase. The point where the rate of increase of the brightness reaches a maximum is judged to be the limb vector. These vectors play a major role in constructing the initial shape model during approach (Section 2.4). Limbs can also be used like landmarks to help determine the spacecraft state, at least in a direction perpendicular to the limb. In SPC they are mainly used during the maplet construction described in Section 3.3 to provide constraining heights during the slope-to-height integration process.

3.3. Constructing a maplet

SPC began more than 30 years ago with the construction of “templates”, or slopes and albedo variations superimposed on flat patches of Martian surface. With a known local Sun direction, the slope variations map directly into brightness variations that can be correlated with imaging data to locate the templates in image space to assist in precision landing. At this stage the precise scale of the slopes was irrelevant because all that mattered for the correlation was the pattern of light and dark. It soon became apparent that the slopes could be integrated to produce topography. The scale of the topography was still a problem, but that could be addressed in several ways, through lower-resolution stereophotogrammetry, knowledge of curvature from initial shape models of small bodies, or from limb observations. These approaches were especially successful if limbs, for example, were also imagined at lower emission angles, so that a scale could be established between the observed limb and an SPC model of the limb, to deconvolve observed surface brightness effects into its constituent albedo and shape effects. While radiometrically corrected images are helpful, it was soon determined that normalization of the imaging data to the initial topography was sufficient to get reasonable consistencies of the surface shapes explored. For early data sets from missions such as Lunar Orbiter, Mariner 10, Viking Orbiter, Phobos 88, radiometrically corrected image data was limited.

A maplet (Figure 4) is a digital topography and albedo map relative to a plane specified by unit vectors U_x, U_y, and U_z and by a maplet vector **V** from the center of the body to the central pixel of the maplet (Figure 3). Grid points (m,n) are spaced by a ground sample distance (GSD) s with m increasing in the U_y direction and n in the U_x direction with $-q \leq m,n \leq q$. Heights $h(m,n)$ are in units of the GSD, so the vector **Z** to any given point on the maplet is

$$\mathbf{Z}(m,n) = \mathbf{V} + s(mU_y+nU_x+h(m,n)U_z) \qquad (15)$$

Testing (Palmer et al. 2022; Weirich et al. 2022; Daly et al. 2022) has shown that best DTM results are obtained when the value of s is chosen to be as small as half the size of the best image GSD input into the SPC process. The values of s can vary across an object depending on the resolution of imaging over an object.

The predicted brightness at a maplet pixel is given by

$$I_p = \lambda A \Phi(\cos(\alpha), \cos(\beta), \gamma) \qquad (16)$$

where α, β, γ are the incident, emission, and phase angles, respectively; A is the (relative) albedo; and λ is a normalization for each image, needed since no attempt is made to radiometrically correct the data. The photometric function Φ can take any form. In the current implementation of SPC, several models exist, including the Lommel-Seeliger model and a modified Lommel-Seeliger developed specifically for the Moon. Barnouin et al. (2020) indicate that the choice of Φ for most reasonable sets of incidences (between 10 and 50 degrees) and emission angles (between 10 and 50 degrees) did not significantly affect resulting maplets DTMs. This indication was based on an extensive study that was completed by the time of Barnouin et al. (2020), while SPC was prepared for use in flight by the OSIRIS-REx mission. The details of these findings are discussed in a manuscript that is being prepared for publication (Palmer et al. 2023, personal communication).

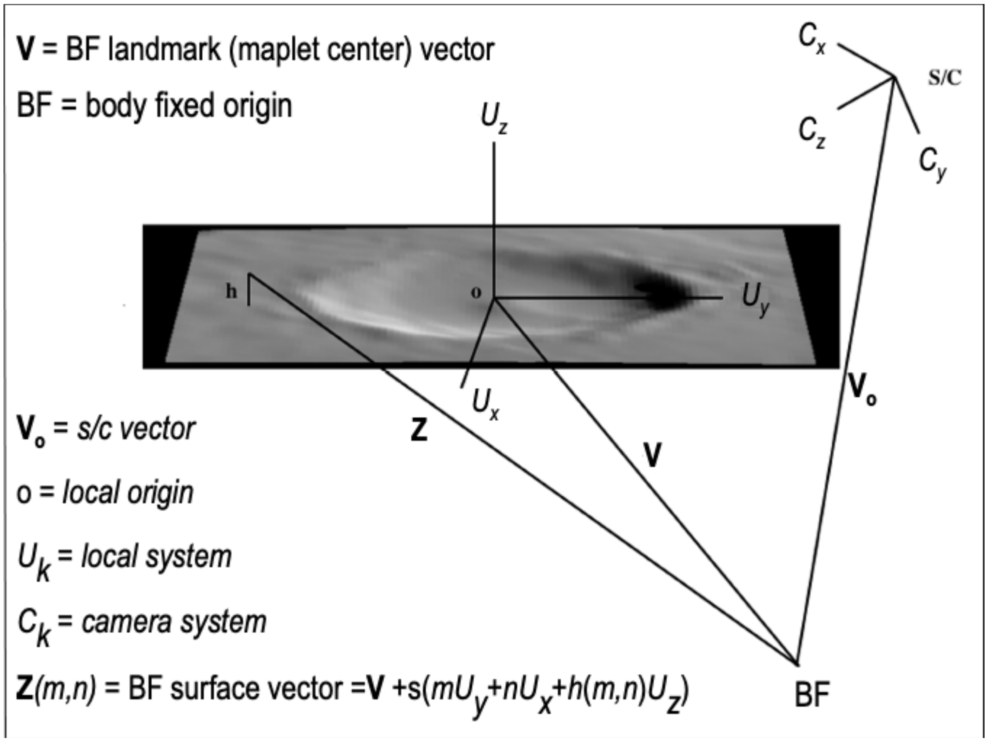

Figure 4: A local DTM or maplet, defining various SPC parameters.

If **C** is the direction from a point on the surface to the camera, **S** is the unit vector toward the Sun, and **N** is the unit normal, then

$$\cos(\alpha) = \mathbf{N}\bullet\mathbf{S} \quad \cos(\beta) = \mathbf{N}\bullet\mathbf{C} \quad \cos(\gamma) = \mathbf{C}\bullet\mathbf{S} \qquad (17)$$

The unit normal vector in the maplet frame is

$$\mathbf{N} = (-t_x, -t_{2y}, 1)/\sqrt{(1+t_x^2+t_y^2)} \qquad (18)$$

where $t_x(m,n)=\partial h/\partial x$ and $t_y(m,n)=\partial h/\partial y$. For notational simplicity, the albedo is also written $A(m,n)=(1+ t_z(m,n))$.

The components of the Sun (s_x, s_y, s_z) and camera (c_x, c_y, c_z) vectors in the maplet ($\mathbf{U_x}, \mathbf{U_y}, \mathbf{U_z}$) frame are found from the body-fixed Sun (**S**), spacecraft-object ($\mathbf{V_0}$), and maplet (**V**) vectors by $s_{x,y,z} = \mathbf{S}\bullet\mathbf{U_{x,y,z}}$ and $c_{x,y,z} = -(\mathbf{V}+\mathbf{V_0})\bullet\mathbf{U_{x,y,z}}$ (normalized), so

$$\cos(\alpha) = (-s_x t_x - s_y t_y + s_z)/\sqrt{(1+t_x^2+t_y^2)}, \ \cos(\beta) = (-c_x t_x - c_y t_y + c_z)/\sqrt{(1+t_x^2+t_x^2)} \qquad (19)$$

Again making use of linear estimation, the slopes and albedos at each maplet pixel are found by minimizing the squared differences between the observed I_o and predicted I_p brightness at each maplet pixel, summed over all images in the maplet:

$$\Sigma_k(I_o - I_p)^2/\sigma^2 = \Sigma_k\,(I_o - \lambda_k(1+t_z)\,\Phi(\cos(\alpha), \cos(\beta), \gamma))/\sigma^2 \qquad (20)$$

giving the linear estimation solution $\delta t_i = M^{-1}_{ij} w_j$ where

$$M_{ij} = \Sigma_k(\partial I_p/\partial t_i)\,(\partial I_p/\partial t_j)/\sigma^2,\quad w_j = \Sigma_k(\partial I_p/\partial t_j)(I_o - I_p)/\sigma^2 \qquad (i,j=x,y,z) \qquad (21)$$

The initial guesses are t_i, and the next estimates are $t_i+\delta t_i$ (i=x,y,z) with multiple iterations performed. The iterations are allowed to approach the final result by adding a weighting toward the prior solution to the diagonal terms M_{ii} of the information matrix. This is a standard technique to avoid divergence without biasing the ultimate result. In the version of SPC that we present here, the partials of the illumination function Φ with respect to cos(α) and cos(β) are numerical, allowing for any choice for Φ. The partials of $\cos(\alpha)$ and $\cos(\beta)$ with respect to t_x and t_y are analytical. After each iteration of the slope/albedo estimation, the RMS brightness residual is displayed to track the convergence of the process.

SPC's albedo solution is only relative, with a different scale for each maplet. It was never intended to do more than prevent brightness variations due to albedo from being interpreted as topographic variations. The sum $1+t_z$ is adjusted after each iteration to average 1 and never exceed 2. The true scale of the predicted brightness is set by λ_k, computed for each image at the beginning of each iteration by requiring that the predicted and observed brightness averaged over the maplet be the same. The weights for the albedo estimation are determined by several parameters set before the processing of a maplet. Some of these are used to de-weight images with very low phase, where the opposition surge may be a problem, and images with high incidence angle, whose brightness variations are dominated by topography. Another parameter sets the maximum range for the albedo in terms of its standard deviation in order to remove outliers. If there is little expected variation in albedo, the brightness variations are primarily due to topography, and the range is set to be relatively small. If there are isolated bright or dark areas that are clearly due to albedo, then the range is set to a larger value to avoid interpreting the albedo extremes as topography.

The treatment of albedo continues to be a work in progress. We have recently increased the upper limit to the maximum of 2.55 set by the byte format of the maplet (.MAP) files. These were designed many years ago to facilitate SPC's use in autonomous navigation (Gaskell, 2001). The average of $1+t_z$ is now fixed at 0.5 instead of 1.0 to provide more room at the upper end for isolated bright areas such as those seen on the dwarf planet Ceres. We have also added an option to further de-weight images with high incidence angles, which have no business participating in albedo determination. This experimental procedure can be turned off or on with a preset parameter.

The slope solution may be consistent with the brightness distribution in the images, but not necessarily with an acceptable topography in that it may not satisfy the curl-free requirement $\partial_x t_y - \partial_y t_x = 0$. It is necessary to find a height distribution for the maplet that is consistent with the slope solution. The relationship between heights at neighboring points and the average slope between them is, with $\boldsymbol{x}$ used as a shorthand for indices m,n in a maplet,

$$h(\boldsymbol{x}+\delta\boldsymbol{x}) - h(\boldsymbol{x}) = \delta\boldsymbol{x}\bullet\boldsymbol{t}(\boldsymbol{x}+\delta\boldsymbol{x}/2) \approx \delta\boldsymbol{x}_k\bullet(\boldsymbol{t}(\boldsymbol{x})+\boldsymbol{t}(\boldsymbol{x}+\delta\boldsymbol{x}))/2 \qquad (22)$$

This relationship is used in a relaxation procedure to iteratively determine the height distribution $h(\boldsymbol{x})$ from the nearest neighbor heights at $\boldsymbol{x}+\delta\boldsymbol{x}_k$ (k=1,4). These nearest neighbor heights are from pixels located in a cross about the pixel defined by $\boldsymbol{x}$. The slopes $\boldsymbol{t}(\boldsymbol{x})$ and possible constraining heights h_c give $h(\mathbf{x})$ as follows:

$$h(\boldsymbol{x}) = [\sum_{k=1,4}(h(\boldsymbol{x}+\delta\boldsymbol{x}_k)-\delta\boldsymbol{x}_k\bullet(\boldsymbol{t}(\boldsymbol{x})+\boldsymbol{t}(\boldsymbol{x}+\delta\boldsymbol{x}_k))/2)+w_c h_c(\boldsymbol{x})]/(w_c+4) \tag{23}$$

where w_c is a small constraining weight. This equation is applied repeatedly to maplet points chosen at random until a converged solution is reached. Constraining heights at randomly selected positions can come from projected overlapping maplets, external maps (derived from other data sources/approaches), the shape model, limb heights (as found from the previous iteration of the topography), vector point clouds (e.g., from lidar data), cross-illumination interpolation in permanently shadowed areas or differential stereo. It is these heights that ultimately set the scale of the topography. If slopes $\boldsymbol{t}$ are not defined at some points, usually because they lie in shadowed areas, they can be filled in either from the shape model or from an external map.

Once the height distribution is determined, it is used to re-compute the slopes and these are fixed to solve for the albedo alone. The RMS brightness residuals then provide a measure of the final GOF. Ultimately, when a maplet is constructed, it is illuminated according to the known imaging geometry and correlated with the orthorectified imaging data for all images in which it appears to find its center's image space locations (control points). After the set of control points has been determined for all maplets, SPC solves for the position of the center of the maplet on the body, the spacecraft position in space, the spacecraft pointing, and of course the topography and albedo across each maplet.

4. Projecting coarser maplets to build higher-resolution maplets

The projection of maplets with coarser spatial resolution (larger GSD) that combine both surface shape and albedo are used to prepare a new set of maplets with finer resolution (smaller GSD; Figure 5). These projections permit estimates of the grid positions and heights of the new maplet. Relative to a new maplet frame U_x, U_y, U_z (eq. 15), the locations and heights of a vector $\mathbf{Z}$ (Figure 4) in an existing reference maplet are

$$x = (\mathbf{Z} - \mathbf{V})\bullet U_x/s,\ y = (\mathbf{Z} - \mathbf{V})\bullet U_y/s,\ h(y,x) = (\mathbf{Z} - \mathbf{V})\bullet U_z/s \tag{24}$$

If the vectors are those at the corners of a reference maplet "cell" $\mathbf{Z}(I,J)$, $\mathbf{Z}(I+1,J)$, $\mathbf{Z}(I,J+1)$, $\mathbf{Z}(I+1,J+1)$, then the projections in eq. 24 are labeled x_k, y_k, and h_k (k=0,3 respectively). A quantity $b(I+\mu,J+\nu)$ in the reference cell is interpolated with

$$b(I+\mu,J+\nu) = B_0 + B_1\mu + B_2\nu + B_3\mu\nu\ [0 \le (\mu,\nu) \le 1]$$

$$\text{with}\ \ B_0 = b_0,\ B_1 = b_1 - b_0,\ B_2 = b_2 - b_0,\ B_3 = b_0 - b_1 - b_2 + b_3 \tag{25}$$

This bilinear interpolation method is used often in SPC for topographic grids, the implicitly connected quadrilateral (ICQ) DTM, and imaging data. Values for μ and ν that project an interior point of the reference cell to a grid point m,n of the new maplet are found by solving

$$m = Y(\mu,\nu) = Y_0 + Y_1\mu + Y_2\nu + Y_3\mu\nu, \quad n = X(\mu,\nu) = X_0 + X_1\mu + X_2\nu + X_3\mu\nu \tag{26}$$

for μ and ν. The height at that point in the new maplet is

$$h(m,n) = H(\mu,\nu) = H_0 + H_1\mu + H_2\nu + H_3\mu\nu \tag{27}$$

The possible values for m and n are limited to the ranges of y_k and x_k, respectively, and to the half-size q of the new maplet. An identical procedure is used to determine the albedo distribution of the new maplet from that of the reference maplet. These projections help to remove the slope ambiguity discussed above and set the scale for higher-resolution topography. A fraction of these projected heights, as determined by a user, provides constraining heights h_c in the slope to height integration eq. 23. We usually try, as much as possible, to choose a reference maplet that completely covers the new maplet. Constraining heights, on the other hand, can come from maplets that only partially cover the new maplet. If no reference maplet completely covers the new maplet, then the missing part is filled with slopes from the DTM, and a second iteration of the maplet generation procedure will fill in the missing area. The same interpolation scheme is used to project maplets onto a DTM as described in the next section, and a DTM constructed from existing maplets can be used in place of the reference maplet above to guarantee complete coverage.

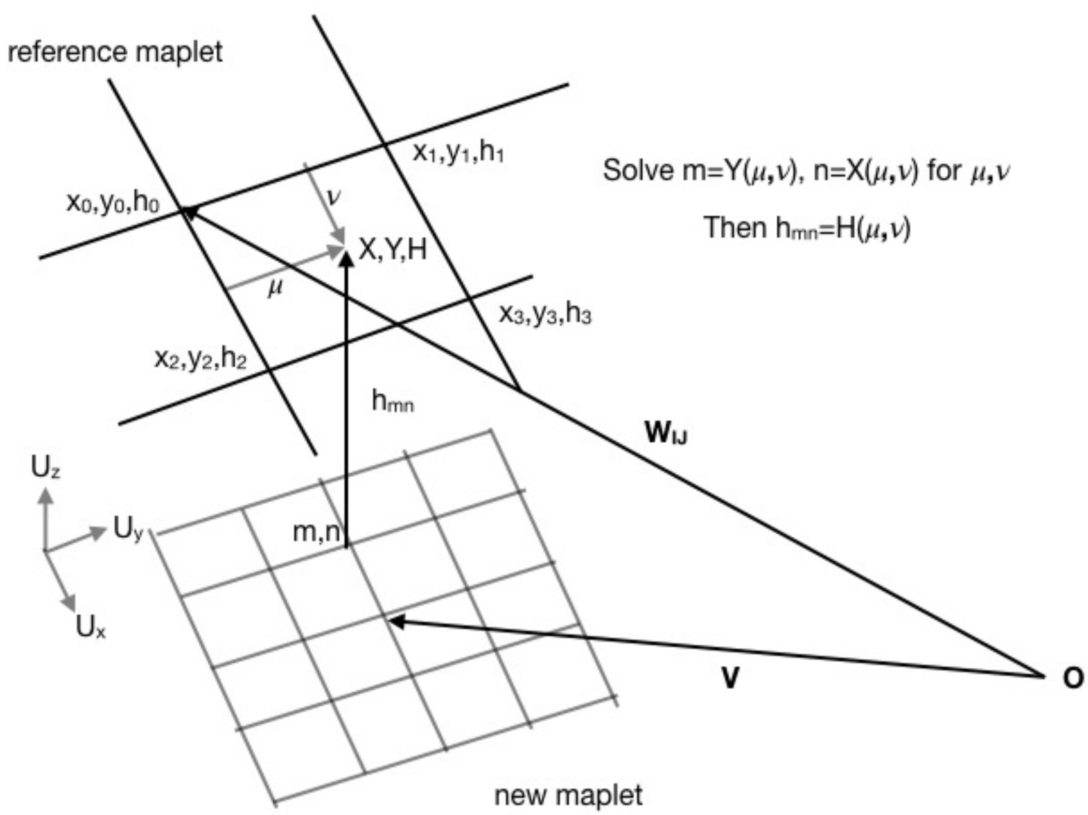

Figure 5. Summary of the projection of a reference maplet onto a new maplet

5. Regional and global models

The maplets created by SPC can be united to make higher-resolution topographic maps across a region, as well as a global DTM. The sections below describe the math behind how these products are made.

5.1. Regional DTMs (bigmaps) constructed from many maplets

It is not uncommon to construct well over 100,000 maplets of varying resolutions, usually much finer than can be captured by even the highest-resolution shape model. For that reason, large "bigmaps" can be constructed using all of the overlapping maplets in a region of interest, or perhaps a selected set. The construction is similar to the projection above, with each maplet projected onto the bigmap frame U_x, U_y, U_z and the weighted average at each grid point providing an initial set of heights $h(m,n)$. Maplets with much coarser resolution than the bigmap are given less weight in the construction with weights $s_0^2/(s_0^2+ s_1^2)$, where s_0 is the DTM GSD and s_1 is the maplet GSD. Users can also limit the maximum GSD of the maplets' input, as well as the distance from the reference DTM. The latter avoids using maplets that are far from where the bigmap is generated. An estimate of the uncertainty at each point in the bigmap is obtained from the standard deviation of the maplet heights that go into the construction of the bigmap.

The location of each maplet's central vector is determined from the images in which it is found by eq. 12 and has an associated error. Sometimes, the maplet can be too high or low relative to surrounding maplets, resulting in a bigmap having "cliffs" at the edges of maplets. This problem is dealt with by randomly choosing a small set of the averaged heights as constraining heights in eq. 23 and using the same weighted average of the slopes to perform the integration. The integration (eq. 23) requires many iterations. The slopes are found by first taking the differentials of eq. 26 and, in two ways, of eq. 27:

$$\delta X = \partial_\mu X \delta\mu + \partial_\nu X \delta\nu, \;\; \delta Y = \partial_\mu Y \delta\mu + \partial_\nu Y \delta\nu \tag{28}$$

$$\delta H = \partial_\mu H \delta\mu + \partial_\nu H \delta\nu, \;\; \delta H = \partial_x \mathrm{h} \delta X + \partial_y \mathrm{h} \delta Y \tag{29}$$

Eqs. 28 are solved for $\delta\mu$ and $\delta\nu$ in terms of δX and δY, and these are substituted into the first of eqs. 29. Comparison of the coefficients of δX and δY with those in the second equation gives

$$\partial_x h = (\partial_\nu H \partial_\mu Y - \partial_\nu Y \partial_\mu H)/(\partial_\nu X \partial_\mu Y - \partial_\nu Y \partial_\mu X) \tag{30}$$

$$\partial_y h = -(\partial_\nu H \partial_\mu X - \partial_\nu X \partial_\mu H)/(\partial_\nu X \partial_\mu Y - \partial_\nu Y \partial_\mu X) \tag{31}$$

Each of the partials is expressed in terms of the bilinear interpolation coefficients. For example, 27 gives $\partial_\nu H = H_2 + H_3\mu$. It may be that the averaged heights alone produce an acceptable DTM. The program BIGMAP has the option of producing such a height-averaged map. BIGMAP also creates a .LMK file for each regional DTM that lists every image used in its creation. The program ALBEDO can be used to find the relative albedo distribution over the entire regional DTM in the same way that albedo was recomputed with fixed topography when generating maplets.

A similar procedure can be used to project a point cloud onto the bigmap frame. In this case, a vector is projected using eq. 24, and initially i and j are taken to be the nearest integers to y and x, respectively. Initially, the slopes in eq. 23 are taken to be zero and a much larger fraction (usually all) of the heights are assigned as constraints. After a number of iterations, the slopes are determined from the intermediate bigmap, and the integration continues. After the bigmap appears to have converged sufficiently where no significant changes are noted, an even cleaner model can be built by using the current slope distribution to correct the heights according to the differences between m and Y, and between n and X. This technique was used to construct bigmaps from OLA data to correct the navigation solutions.

5.2. Global DTMs constructed from many maplets

The shapes of many bodies (e.g., Vesta, the Moon, Mercury) can be represented, at least to the scale we are considering, as a single radius as a function of latitude and longitude. Put another way, a line from the center of the body in any direction will pierce the surface only once. For some of these bodies, SPC was used to creates a set of bigmaps called Z-maps centered at every five degrees of latitude and longitude labeled as Z(N/S)abcd, where the central latitude is 5ab N or S with east longitude of 5cd with (ab=0,18, cd=0,71). There is no ZS00cd, and the labels need not be spaced by 1 to ensure full coverage. In the current software, bigmaps can be up to 5001x5001 pixels. The program REGISTER, which produces the first correction to the spacecraft state when a new image is introduced, automatically finds the existing Z-map that is most likely to overlap the image, and this can be used to register that image in place of the usual shape model. SPC has a utility program called SPHEREMAPB that uses the Z-maps to construct global maps for the topographic data in equirectangular, stereographic, or orthographic projection, the latter two for polar regions. The output consists of heights relative to an appropriately chosen sphere as a function of latitude and longitude. The computation is done one line at a time so the constructed maps can be as large as desired. This approach was not used for products generated by OSIRIS-REx at Bennu (Barnouin et al. 2020). Instead, SPC-derived vertices were used with other tools such as The Generic Mapping Tools (Wessel et al., 2019) to build simple cylindrical maps.

Eros was the first body modeled that had multiple radii in a single direction. Typical projections are unsuitable. Instead of using the height along a normal to a sphere as a way of specifying surface vectors, we created an initial non-spherical model and to extend its surface normals as a way of defining new surface points. An efficient labeling scheme already existed for such models, an outgrowth of a scheme to produce small bodies at arbitrarily high resolution that had been used to construct a fake Eros for NEAR navigation studies prior to the encounter. It was good fortune that this technique was developed before it was really needed for the Hayabusa encounter with asteroid Itokawa.

5.2.1.The ICQ format

Similar to how a maplet ensemble can be brought together to construct a bigmap, the maplets can also be united to construct a global DTM. SPC is set up to use the ICQ format for its shape models. The vectors are labeled and connected to each other as though they were grid points i,j on the faces f of a cube as in Figure 6, so their labels are i, j, and f where (i=0,q; j=0,q; f=1,6), and no separate facet table is necessary. The parameter q is conventionally, but not necessarily, taken to be a power of 2, and models are constructed with increasing detail by repeated doubling of q. It is a simple matter to convert an ICQ model to a triangular facet model if desired (See NAIF DSK routines that allow converting from ICQ to common OBJ formats at naif.jpl.nasa.gov). Although the six cube faces have $6(q+1)^2$ labels, the shape model itself has only $6q^2+2$ unique vectors because of duplicate labels on the edges and corners. The SPC implementation used here is configured so that if a change is made to a vector with an edge or corner label, all duplicate vectors are changed accordingly. If an index i or j on one face is incremented and becomes less than 0 or greater than q, then the label is mapped onto a different face, with new indices i and j between 0 and q.

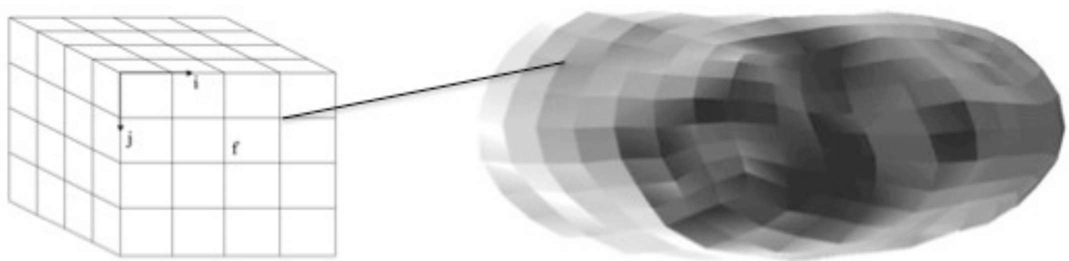

Figure 6. Implicitly connected quadrilateral labels (q = 4) and a similarly connected shape model.

The quadrilateral cells can be projected onto maplets using eq. 24, although care must be taken not to look through the body and use cells on the far side or perhaps on other lobes if the body is complex. Thus an initial shape model can be used to set the topographic scale of the initial set of maplets through equation 16.

5.2.2. Building the global digital terrain model

Once a set of maplets has been constructed, the shape model can be refined by a procedure similar to that described in Section 4. This is slightly different from projection onto a maplet, however, because the projection is in the direction of the surface normal of an initial shape instead of in a constant direction Z. As the GSD of the shape model becomes smaller, the normal is usually defined over baselines that shrink less rapidly than the GSD. At each point **P** of an initial shape model, the surface normal **N** is extended until it pierces one of the maplets. The piercing point is found iteratively by equating the maplet position from eq. 15 with the vector $\mathbf{P} + \alpha\mathbf{N}$:

$$\mathbf{P} + \alpha\mathbf{N} = \mathbf{V} + s(\mathrm{m}U_y + nU_x + h(m,n)U_z) \quad (32)$$

For a given α, the maplet coordinates of the solution and the new estimate of α using these values are

$$x = (\mathbf{P}-\mathbf{V}+ \alpha\mathbf{N})\bullet U_x/s,\ y = (\mathbf{P}-\mathbf{V}+ \alpha\mathbf{N})\bullet U_y/s,\ \alpha = [(\mathbf{V}-\mathbf{P})\bullet U_z + h(\mathrm{y},\mathrm{x})]/(\mathbf{N}\bullet U_z) \quad (33)$$

where $h(y,x)$ is determined with bilinear interpolation on the m,n cell with $y=m+\mu$, $x=n+\nu$, and μ,ν between 0 and 1.The weighted average $\mathbf{P}+<\alpha>\mathbf{N}$ over all maplet piercings provides a new surface vector. Each maplet piercing also has an associated slope that is determined by bilinear interpolation of the cell's corner points and is used with eq. 18 to compute the normal at that point. The average of these local normals **n** is also saved. While this result could be taken as the finished shape model, there is the possibility of discontinuities at maplet boundaries as in Section 6. The equivalent to eq. 23 is

$$\alpha_0 = [\sum_{k=1,4}(\mathbf{P}_k-\mathbf{P}_0+ \alpha_k\mathbf{N_k})\bullet(\mathbf{n}_k+\mathbf{n}_0)/\mathbf{N}_0\bullet(\mathbf{n}_k+\mathbf{n}_0)+w_c\alpha_{00}]/(w_c+4) \qquad (34)$$

$\mathbf{P}_0$ is the nominal surface vector, $\mathbf{P}_k$ are the four nearest neighbors, $\mathbf{N}_0$ and $\mathbf{N}_k$ are the associated unit normals, $\mathbf{n}_k$ are the local normals, and α_{00} is the original α_0 before iteration. For most points, w_c is zero, but for a small number of randomly selected points it is given a small nonzero value. Eq. 34 is iterated many times at random points to provide the final set of shape vectors $\mathbf{P}+ \alpha\mathbf{N}$. The standard deviation of the α for each maplet piercing is tracked for each point of the global DTM, providing a global uncertainty map that is used to identify areas that might need further work.

Instead of iterating eq. 33 to find piercing points, the procedure described in Section 4 could be used, with each vector **P** equivalent to the central vector of a bigmap and **N** equivalent to its $\mathbf{U_z}$. This is relatively inefficient because each bigmap contains only one point, and the resulting process takes about four times as long. Notice that in Section 5.1, the slopes were found by differentiating the bilinear interpolation of the heights, whereas in this section the bilinear interpolation of the slopes was used. Either method can be used for constructing bigmaps, and it is still not clear which is best, but the slope interpolation seems to provide steeper slopes around boulders.

6. Incorporating altimetric data to improve the SPC solution

Although SPC excels at uniting images at a variety of pixel scales and imaging conditions together to derive topography, it has limitations. Images rely on solar illumination, so areas that are not illuminated in any images cannot be modeled accurately. Many of the small bodies (as well as some large planets such as Mercury) visited so far by spacecraft possess a pole orientation that leads to no seasonal variation in illumination. Some areas near the north and south poles can be in permanent shadow, and some areas may never be imaged during a mission due to limited imaging opportunities (e.g., flyby missions). Further, SPC tends to smooth topography when the surface changes quickly over short lateral scales, where steep slopes exist (e.g., boulder edges; Barnouin et al. 2020).

Use of SPC can also lead to the size/distance degeneracy discussed in the introduction, because of the lack of an absolute measurement of distance. For small bodies, proximity navigation is accomplished by using the "known" maplet vectors and their image space locations to solve for the spacecraft state. The entire procedure is subject to a scale adjustment. All vectors can be scaled up or down by a small fraction and still yield a consistent solution.

If available, altimetric data can be incorporated to improve maplet topography in shadowed or rugged areas. In addition, the size/distance degeneracy can be resolved by applying laser ranges. The measured range to the surface is used to correct the range to the body center, and the fractional change is then applied to all vectors.

Shape modeling efforts for Bennu made use of altimetric data to improve the topographic solution and reduce uncertainties in shape model scale. Bennu's axis is tilted only about 2.4° from its orbital plane, so there are areas at high latitudes that are never illuminated in images. Bennu's surface is littered with boulders up to tens of meters across, creating a rough terrain with many high slopes (Lauretta et al., 2019). Lidar ranging data were collected by the OSIRIS-REx Laser Altimeter (OLA) (Daly et al., 2017;). The OLA product used to incorporate the laser altimetry data into SPC was a global set of 7992 20-cm-GSD regional DTMs or "mapolas" constructed from OLA points clouds using a spacecraft trajectory from the Flight Dynamics team, with some modification to minimize errors between individual scans (Seabrook et al., 2019, 2022 [this focus issue]; Barnouin et al., 2019, 2020; Daly, M.G. et al, 2020). Mapolas are DTMs stored in the same format as standard SPC maplets, but where the relative albedo is set to 1, because OLA did not measure surface albedo directly (Daly et al. 2020). The following subsections elaborate on how mapolas were added to the SPC data set.

6.1. SPC/laser altimetry hybrid models (SPCOLA)

OLA data provide ranges to the surface over the whole body, illuminated or not, that can be used to construct an independent topographic model. Vectors from that model can be used to provide constraining heights to SPC's slope-to-height integration and to help fill in these dark areas and improve modeled rock heights and edges. The approach of combining traditional SPC techniques and OLA data is called SPCOLA. Figure 7 shows how the SPCOLA approach can improve the derived topography and better model rock heights.

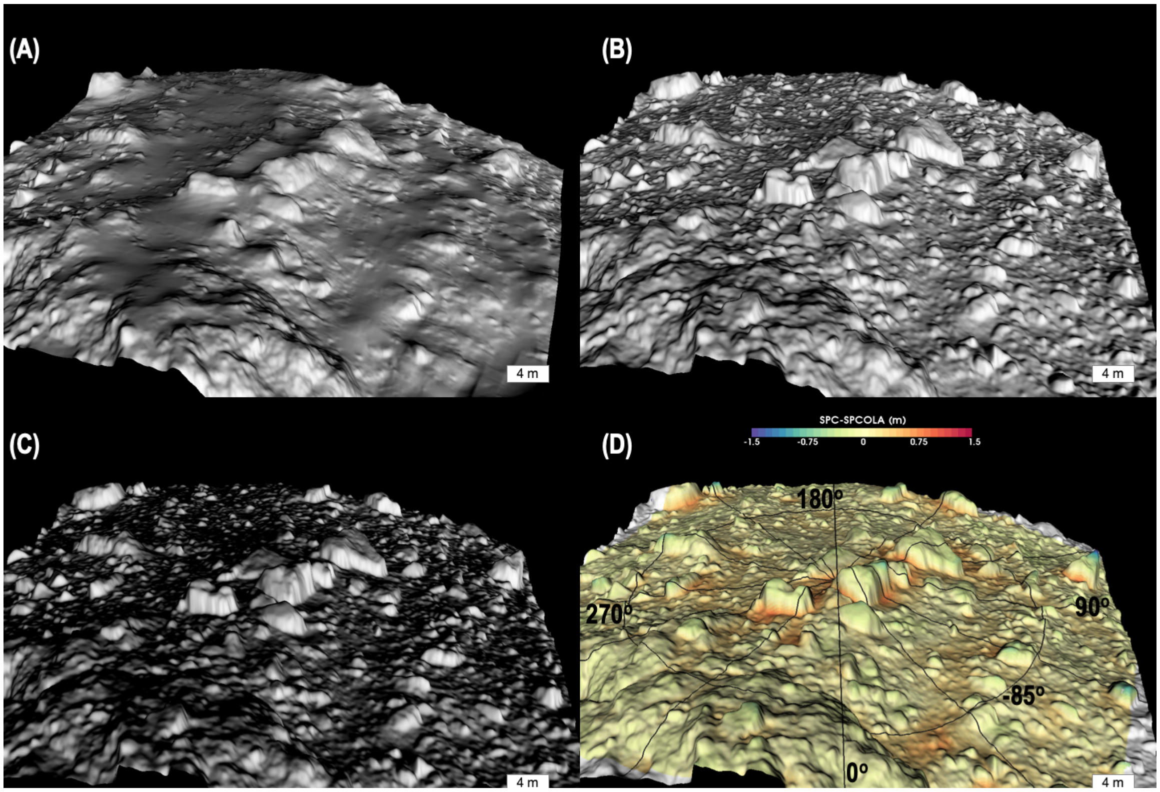

Figure 7. Bennu's south pole modeled using SPC only (A) and with the combined SPCOLA technique, using mapolas for constraining heights (B). Smooth areas seen in the SPC model, show more relief when the OLA data are included primarily because images of Bennu's south pole are poorly illuminated, as illustrated in (C) where the model in (B) is viewed using current lighting conditions on Bennu. On average, differences between the two products are fairly small (<0.2m). The addition of OLA removes smooth aprons around rocks and models the tops of rocks better, as seen in the difference map (D). Bennu products using SPC or OLA only are compared in detail in Al Asad et al., (2021) and are not shown here. But differences between OLA and SPC are usually smaller than those seen between (A) and (B) shown here, mostly because lighting conditions are better elsewhere on the asteroid.

The mapolas were added to the SPC data set, and their centers in the images determined in the usual way by correlating rendered mapolas with orthorectified imaging data. The mapolas' heights were used unchanged, but we assumed that the absolute location of the central vectors of these mapolas were not in the correct position. We therefore solved for them with eq. 12. The changes in the central vectors were fit to an affine transformation consisting of translations of about 5 cm per axis, rotations of about 0.002° per axis, and a scale change of about 0.05%. Nonuniform scaling and shear were not considered. The standard deviation of the fit was about 4 cm per axis, within the known absolute uncertainties for OLA and these Bennu SPC models. Once the central vectors were fixed, the albedo distribution ($1+t_z$) was determined for each mapola by using eq. 21 with t_x and t_y determined from the new OLA-influenced shape, mirroring the final step in the maplet construction discussed above. This allowed a better determination of the mapolas' overlaps with other image-derived maplets, an important part of the geometry solution.

A separate approach was attempted whereby 640 individual OLA scans were added to the SPC solution. Each one of these scans included >1 million vectors each, describing an expansive 100 m by 100 m patch of the surface of Bennu, where the vectors are separated by a GSD of 5–7 cm. These can be directly correlated with corresponding SPC patches to obtain a transformation from the OLA coordinates to SPC's with an almost identical fit as the mapola approach. The vectors could be used directly to provide constraining heights for the slope-to-height integrations in eq. 23. In the end, it was decided to use the mapola approach only, because the data volume from those products was more manageable. Any adjustment using the OLA scans for pole update, for example, required month-long iterations. Further, these vectors produced too much noise in the higher-resolution SPC maplet solutions derived from these mapolas and other lower-resolution SPC-derived maplets. These mapolas have reduced noise because they include a median height for the all the OLA returns available in a given pixel (see Barnouin et al., 2020, for more details). The original set of individual mapolas that are including in the SPCOLA results are available as .fits files in the Small Body Mapping Tool, downloadable at sbmt.jhuapl.edu. They participate with other SPC-maplets in the final solution of the SPCOLA models, with their central vectors and orientations changing with each iteration or due to any changes in the reference frame, while maintaining their provided heights.

6.2. Using altimetry data to scale small bodies accurately

In the case of a rendezvous mission, where the spacecraft slowly approaches an asteroid, the initial scale of a small body and the landmarks used for proximity navigation are set by observing its increase in angular size with time. The size of the small body is determined by combining a camera model and Doppler-determined relative velocity. Because the approach is slow (meters to centimeters per second), uncertainties in the spacecraft velocity and the ephemeris of the target object can be significant and yield errors in the overall scale of a small body to perhaps a tenth of a percent (Gaskell et al. 2006). If all linear scales including velocities and accelerations possess some uncertainty ε, and are therefore multiplied by an unknown scaling factor, say $(1+\varepsilon)$, then several equally valid solutions for the asteroid can be reached.

To circumvent such a scaling uncertainty, SPC can make use of additional data. Both the NEAR (Cole et al., 1997) and Hayabusa (Mukai et al. 2002) missions were equipped with a laser ranger approximately co-boresighted with the camera. Once a solution for landmarks and spacecraft state was achieved, it was possible to determine the vector to the surface point intercepted by the laser ranger, a known fixed pixel/line location in an image, the spacecraft position at the imaging time, and therefore the range r from that surface point to the spacecraft. If the measured lidar range to the surface at that time is $(1+\varepsilon)r$, then multiplying all linear scales in the SPC solution by $(1+\varepsilon)$ yields a solution consistent with the laser ranging results. Such an approach was successfully employed during the Hayabusa mission (Gaskell et al., 2008; Barnouin-Jha et al., 2009).

A different approach was taken to assess any size issues during the OSIRIS-REX mission because OLA is a scanning altimeter. During one of the fly-over phases (Detailed

Survey; Lauretta et al. 2017, 2021), OLA collected 13 scans simultaneously with dense sets of OCAMS images, the only time during the mission that this was the case. These scans included estimates of the body-fixed spacecraft positions and surface intercept points derived from a reference ephemeris. By using an SPC-derived trajectory solution in place of the reference, a new set of surface points was determined. Because in this case there is no longer a single image pixel tied to a single lidar spot, as was the case for single-shot lidar, a first bigmap is made from the ensemble of SPC maplets and centered at the image's central pixel. A second bigmap is made from the lidar point cloud using the same reference frame central vector $\mathbf{V}$ and GSD s as the first bigmap. If $\mathbf{V_c}$ is one of the vectors from the OLA point cloud, then its x and y coordinates and its height are

$$x = (\mathbf{V_c} - \mathbf{V})\bullet\mathbf{U_x}/s,\ y = (\mathbf{V_c} - \mathbf{V})\bullet\mathbf{U_y}/\mathrm{s},\ h_c(m,n) = (\mathbf{V_c} - \mathbf{V})\bullet\mathbf{U_x}/s \qquad (35)$$

where m and n are the integers nearest to y and x, respectively. Many of the m,n bins contain no projected vectors, so the second bigmap is constructed by using the heights in eq. 35 as constraining heights in eq. 23. The actual heights h and slopes $\mathbf{t}$ are initially set to zero. After a number of iterations, the ensemble of new heights h is used to produce new slopes $\mathbf{t}$, and the iteration proceeds once more. If desired, the current slope estimates can be used to refine the constraining heights in eq. 35:

$$h_c(m,n) = (\mathbf{V_c} - \mathbf{V})\bullet\mathbf{U_x}/s + t_2(m,n)(m - y) + t_1(m,n)(n - x) \qquad (36)$$

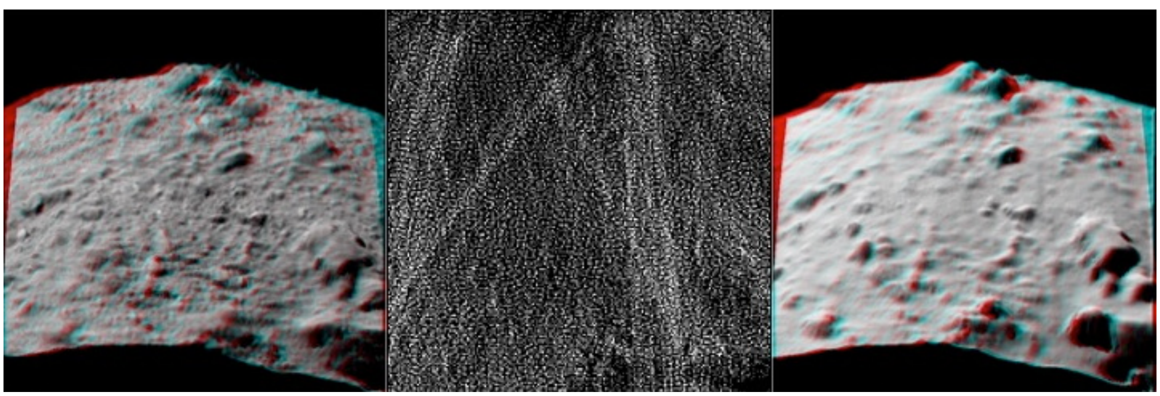

Figure 8. SPC and OLA bigmaps used to improve navigation and global size. From left to right: bigmap from SPC; OLA point cloud coverage; bigmap from OLA vectors. The OLA point cloud is viewed looking vertical down on the surface shown on the right and left.

Two 100 m by 100 m bigmaps were created around the central pixel of each detailed survey image, one from the set of maplets and the other from the OLA point cloud (Figure 8). The bigmaps were about twice the PolyCam footprint and half that of MapCam and had a GSD of 50 cm, close to the OLA high-energy laser transmitter's spot size. Correlation of the SPC and OLA bigmaps provided range residuals along with an offset indicating a difference of about 0.01° in the OLA and SPC prime meridians. The average fractional range residuals for each of the daily scans had a minimum of $\varepsilon = -0.000070$ to a maximum of $\varepsilon = +0.000250$, with uncertainties of about 0.00005 for each day. Included in the uncertainty value is a longitudinal variation that may indicate a slight offset of the center, but the overall asteroid size corrections suggested by the ε, –1.8 cm to +6.0 cm, are remarkably small and validate the SPC-derived size of Bennu. There is a noticeable variation with time of day, with the largest ε at 6:00 am and 6:00 pm local time and the smallest at 12:30 pm. The cause for this variation remains a mystery.

7. Software implementation

There have been many versions of the software over the years, and it is important to use a single one for a given project. The engineering version used on the OSIRIS-REx mission was that used for the ROSETTA comet encounter (2014), with a few cosmetic changes and bug fixes. Although the core philosophy behind our implementation of SPC (linear estimation, and the use of stereo and photoclinometry) is unchanged, over 70 numbered versions of the software track the evolution of the science versions since then. Most of these updates relate to the use of additional datatypes.

The core file structures for our current implementation of SPC have existed for two decades (Gaskell, 2001). Landmark (.LMK) files describe the locations and orientations of maplets, the pixel/line locations of the maplets in images and on image limbs, and the relative locations of overlapping maplets. Maplet (.MAP) files save the heights and relative albedos describing the maplet surface shape. Summary (.SUM) files contain the camera parameters and spacecraft state solution for each image and the pixel/line location of all maplets in the image and on image limbs. Nominal (.NOM) files contain the spacecraft state specified by the SPICE kernels. Spacecraft images (.DAT files) are stripped of any header information, and are byte or unsigned short, most significant bit files with no headers.

The core SPC software has changed since 2001 from a monolithic octopus of code to programs that perform specific functions. Here, we briefly introduce some of these programs; see Palmer et al. (2022) for more detailed descriptions. PROCESS_FITS or PROCESS_IMG converts mission optical data to the SPC image format (.DAT) and saves ancillary information for the creation of .NOM and initial .SUM files. MAKE_SUMFILES uses SPICE data to create .NOM files and initial .SUM files. REGISTER, while becoming an octopus in its own right, has the primary function of providing an initial spacecraft state solution for each image by aligning the image with an initial shape model. It is also used to correct the range to the body during approach, to find an initial pole solution, and, in conjunction with the limb program LIMBER, to refine the initial shape model. AUTOREGISTER is used to further refine the spacecraft state by locating exiting maplets in new images. LITHOS, the workhorse of SPC, constructs the maplets and the landmark files from the spacecraft states and imaging data as described in Section 3. GEOMETRY solves for the landmark vectors and spacecraft states using the methods of Section 3. RESIDUALS finds the differences between observed and predicted image space positions of the landmarks, displays them in ways to flag possible misalignments, and computes the final linearized RMS residual.

Many utility programs have been developed to better exploit the results from the core SPC software. Among these are BIGMAPS and DENSIFY, which construct high-resolution topographic maps and ICQ DTMs as described in Section 5, and software to turn a set of topographic maps into global gridded topography in various projections. The albedo portion of a maplet is a relative distribution designed to better identify the topography signal in the data. Combining these individual signals in making a larger map may be questionable, so an ALBEDO program was constructed to find the relative albedo signal over an entire topographic map.

8. Conclusion

SPC is a powerful approach for accurately modeling the shape of planets and irregularly shaped small bodies (Barnouin-Jha et al., 2008; Jorda et al., 2016; Perry et al., 2015; Barnouin et al., 2019; Al Asad et al. 2021; Palmer et al., 2022), even when limited data are available (Daly et al. 2022). This paper explains the mathematics behind the SPC method. At its essence, SPC uses images and a priori estimates of a spacecraft trajectory to solve for the surface shape and relative albedo of a target object, and a provides reconstructed spacecraft position and pointing. The images provide both stereo-parallax and shading information that allow estimating the surface shape in three dimensions. Linear estimation is at the mathematical center of SPC. In addition to images, SPC can accept and has taken advantage of many data types with excellent results, including limb information and laser altimetry.

The original goal of SPC was to provide easily identifiable control points for spacecraft navigation and target shape determination. The maplets used to define the control points can exhibit topography at levels close to the resolution of the best input images. The quality of the data plays a role in the success of SPC and can be limited by physical or mission constraints. In many cases (Mercury, Ceres, Itokawa, Bennu, etc.) there is little seasonal variation and some areas in the north and south are never illuminated. In these cases, illumination near the equator is also mainly in the east-west direction, giving little information about north-south slopes. Inclusion of auxiliary data such as laser altimetry can help with the solutions and was used for NEAR, Hayabusa, and OSIRIS-REx analysis. In some cases, such as the DAWN mission, the cameras had sufficient dynamic range to produce data in the permanently shadowed areas from secondary illumination. An experimental procedure has been developed for building maplets from these data.

Shape models constructed from the maplets are true three-dimensional representations, whereas bigmaps and the maplets themselves are 2.5-dimensional — heights relative to a planar grid. The imaging data used in SPC translates into slopes rather than heights, and sharp height changes or even overhangs tend to be smoothed down by the slope-to-height integration procedure. The use of many overlapping maplets helps to some degree because there is variation in the orientations of the reference planes. A possible area for experimentation on this front would be to create a number of otherwise identical maplets with different reference planes.

Each new mission seems to introduce one or more wrinkles to test SPC. In the case of OSIRIS-REx, the navigation cameras used rolling shutters and this capability is now included in SPC. The official version of SPC used on OSIRIS-REx dates from mid-2014 at the beginning of the ROSETTA mission's comet encounter. It was necessary to modify that version of SPC to handle and solve for non-principal axis rotation. This new feature was used to characterize the changing pole and rotation rate of the comet 67P/Churyumov–Gerasimenko. Many years ago, an alternate version of SPC designed for line array cameras was developed. Line array data generally have much higher resolution than framing camera data but do not have the advantage of a rigid connection between image points. Lately, several bodies (Phobos, Deimos, Pluto, and Charon) have been studied that have both framing camera and line array data. The .SUM files for line array cameras contain extra information to determine the s/c state for each line of the image. The latest version of SPC incorporates the mathematical methods for handling this line array data, which previously existed in a separate experimental module.

As an example, a near-final application of SPC on OSIRIS-REx was the construction of the spacecraft trajectory during the Touch-and-Go (TAG) sample collection maneuver. Autonomous navigation during this phase was accomplished by natural feature tracking (NFT; Olds et al. 2022; Norman et al., 2022; Mario et al. 2022) using a hundred or so SPC derived feature maps. Here we show an estimate of the trajectory of the S/C during TAG. We use all the landmarks that went into the our SPC terrain solution before TAG, making use of nearly all the images captured by nearly all the cameras on the S/C employed until just before TAG. Afterwards, when the spacecraft had retreated far enough, we use visible landmarks undisturbed by the sampling and thrusting. The spacecraft positions and velocities determined by the procedures of Section 3.1 allowed a precise trajectory determination to within a few centimeters, and a dynamical model fitting to these data enabled the interpolation in the interval when the surface was obscured following the ascent burn. An anaglyph of the resulting trajectory appears in Figure 9. The checkpoint burn cancels the orbital velocity, and the spacecraft begins its descent toward Bennu. The matchpoint burn adjusts the horizontal velocity to match the rotation of the body. Just after TAG, the ascent burn starts moving OSIRIS-REx away from Bennu. The last use of SPC at Bennu was performed during a subsequent flyover of the TAG site to assess surface changes. The SPC results are discussed extensively in Lauretta et al. (2022).

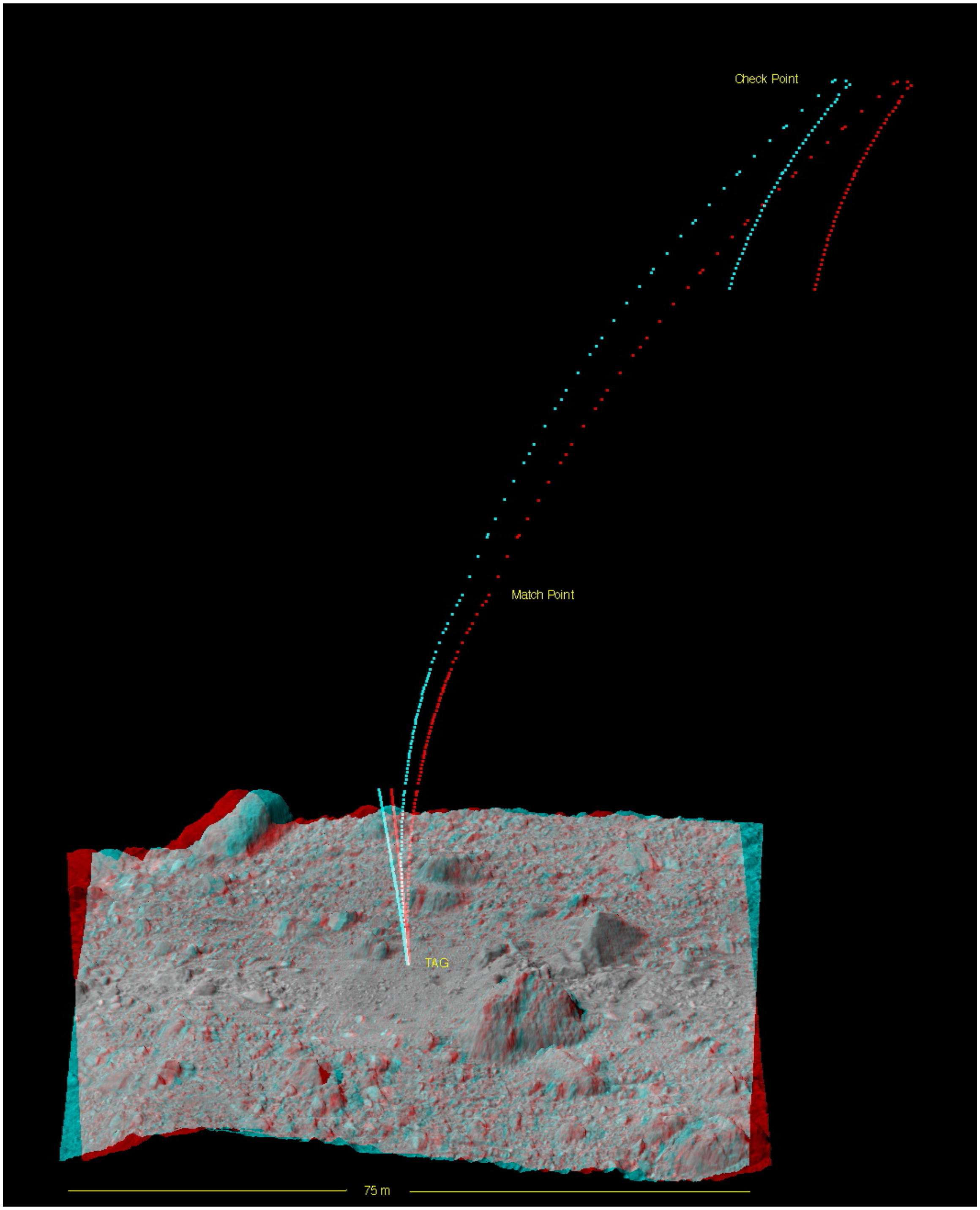

Figure 10. Anaglyph of SPC determined trajectory for the OSIRIS-Rex sample collection operations.

Acknowledgments:

This material is based upon work supported by NASA under Contract NNM10AA11C issued through the New Frontiers Program. OLA and support for the Canadian contributors were provided by the Canadian Space Agency. We are grateful to the entire OSIRIS-REx Team for making the encounter with Bennu possible. All data

from the OSIRIS-REx mission are available via the Planetary Data System (PDS) at https://sbn.psi.edu/pds/resource/orex/. Shape models of Bennu are available via the PDS or by downloading the Small Body Mapping Tool at http://sbmt.jhuapl.edu/. License of the SPC software suite is available from the Planetary Science Institute at https://spc.psi.edu. Please contact Eric Palmer (epalmer@psi.edu) for information of access, training and the fee schedule.

References:

Acton Jr, 1996. Ancillary data services of NASA's Navigation and Ancillary Information Facility. PSS 44, 65–70. https://doi.org/10.1016/0032-0633(95)00107-7

Acton, C. et al. 2018. A look towards the future in the handling of space science mission geometry. PSS 150, 9–12. https://doi.org/10.1016/j.pss.2017.02.013

Adam, C., McCarthy, L., Leonard, J et al., 2022. Stereophotoclinometry for OSIRIS-REx Spacecraft Navigation. PSS in review.

Al Asad, M.M., Philpott, L.C., Johnson, C.L. et al., 2021. Validation of Stereophotoclinometric Shape Models of Asteroid (101955) Bennu during the OSIRIS-REx Mission. The Planetary Science Journal 2, 82. https://doi.org/10.3847/PSJ/abe4dc

Barnouin-Jha, O.S., Cheng, A.F., Mukai, T. et al., 2008. Small-scale topography of 25143 Itokawa from the Hayabusa laser altimeter. Icarus 198, 108–124. https://doi.org/10.1016/j.icarus.2008.05.026

Barnouin, O.S. et al., 2019. Shape of (101955) Bennu indicative of a rubble pile with internal stiffness. Nat. Geosci. 12, 247–252.

Barnouin, O.S. et al., 2020. Digital terrain mapping by the OSIRIS-REx mission. *Planetary and Space Science*, 180, 104764.

Barnouin, O.S., Jawin E.R., Daly, R.T., et al., 2022. Geologic Context of the OSIRIS-REx Sample Site from High-resolution Topography and Imaging. PSJ, 3, 75.

Bos, B.J., Ravine, M.A., Caplinger, M., et al., 2018. Touch And Go Camera System (TAGCAMS) for the OSIRIS-REx Asteroid Sample Return Mission. Space Science Reviews 214, 37. https://doi.org/10.1007/s11214-017-0465-2

Bos, B.J., Nelson, D.S., Pelgrift, J.Y. et al., 2020. In-Flight Calibration and Performance of the OSIRIS-REx Touch And Go Camera System (TAGCAMS). Space Science Reviews 216, 71. https://doi.org/10.1007/s11214-020-00682-x

Cole, T.D., Boies, M.T., El-Dinary, A.S., Cheng, A., Zuber, M.T., Smith, D.E., 1997. The Near-Earth Asteroid Rendezvous laser altimeter. Space Science Reviews 82, 217–253. https://doi.org/10.1023/A:1005056828065

Daly, M.G., Barnouin, O.S., Dickinson, et al., 2017. The OSIRIS-REx Laser Altimeter (OLA) Investigation and Instrument. Space Science Reviews 212, 899–924. https://doi.org/10.1007/s11214-017-0375-3

Daly, M.G., Barnouin, O.S., Seabrook, J.A., et al., 2020. Hemispherical differences in the shape and topography of asteroid (101955) Bennu. Science Advances 6. https://doi.org/10.1126/sciadv.abd3649

Daly R.T., Ernst CM, Gaskell RW, et al (2018) New Stereophotoclinometry Shape Models for Irregularly Shaped Saturnian Satellites. Lunar and Planetary Science Conference 49, #1053.

Daly R.T., Ernst. C.M., Barnouin, O.S. et al (2022) Shape modeling of Dimorphos for the Double Asteroid Redirection Test (DART). PSJ, in press.

Ernst CM, Gaskell RW, Daly RT, Barnouin, OS, Thomas, PC (2019) A Stereophotoclinometry Model of Comet Tempel 1. Lunar and Planetary Science Conference 50, #2640.

Ernst, C.M. et al., 2022, High-resolution shape models of Phobos and Deimos from stereophotoclinometry, *Earth, Planets and Space,* in review.

Gaskell, R., 2001. Automated Landmark Identification for Spacecraft Navigation. AAS paper 01-422, AAS/AIAA Astrodynamics Specialists Conf., August. 2001, Quebec City, PQ, Canada.

Gaskell RW (2008) Gaskell Eros Shape Model V1.0. NEAR-A-MSI-5-EROSSHAPE-V1.0. NASA Planetary Data System.

Gaskell, Robert W., 2011. Optical navigation near small bodies. *Proc. 21st AAS/AIAA Space Flight Mechanics Meet.* 140 (11–220), 13.

Gaskell, R.W., 2012. SPC Shape and Topography of Vesta from DAWN Imaging Data DPS, 44, 209.03.

Gaskell RW, 2013. Gaskell Phoebe Shape Model V2.0, CO-SA-ISSNA-5-PHOEBESHAPE-V2.0. NASA Planetary Data System.

Gaskell, R.W., 2020. Gaskell Phobos Shape Model V1.0. NASA Planetary Data System 67. https://doi.org/10.26033/xzv5-bw95

Gaskell, R.W., Jorda, L., Palmer, E., Jackman, C., Capanna, C., Hviid, S., Gutiérrez, P., 2014. Comet 67P/CG: Preliminary Shape and Topography from SPC 46, DPS, 209.04.

Gaskell, R.W., Barnouin-Jha, O.S., Scheeres, D.J., Konopliv, A.S., Mukai, T., Abe, S., Saito, J., et al., 2008. Characterizing and navigating small bodies with imaging data. *Meteorit. Planet. Sci.* 43 (6), 1049–1061.

Gaskell, R.W., Barnouin-Jha, O.S., Scheeres, D.J., Mukai, T., Hirata, N., Abe, S., Saito, J., et al., 2006. Landmark navigation studies and target characterization in the Hayabusa encounter with Itokawa.. In: *AIAA/Aas Astrodynamics Specialist Conference and Exhibit*. American Institute of Aeronautics, Reston, Virginia (Astronautics).

Gaskell R, Mastrodemos N, Hayward R, Rosiek M (2011) SPC Topography from Clementine Images. Lunar and Planetary Science Conference 42, #2535.

Gaskell, R.W., Synnott, S.P., McEwen, A.S., Schaber, G.G., 1988. Large-scale topography of Io - implications for internal structure and heat transfer. *Geophys. Res. Lett.* 15 (6), 581–584.

Golish, D.R. et al. (2020). Ground and In-Flight Calibration of the OSIRIS-REx Camera Suite. Space Sci. Rev. 216, 12.

Jorda L, Gaskell R, Capanna C, et al (2016) The global shape, density and rotation of Comet 67P/Churyumov-Gerasimenko from preperihelion Rosetta/OSIRIS observations. Icarus 277:257–278. doi: 10.1016/j.icarus.2016.05.002

Lauretta, D.S. et al. (2017). OSIRIS-REx: Sample Return from Asteroid (101955) Bennu. Space Sci. Rev. 212, 925–984.

Lauretta, D.S., DellaGiustina, D.N. et al. (2019). The unexpected surface of asteroid (101955) Bennu. Nature 568, 55–60.

Lauretta, D. S. et al. (2021). OSIRIS-REx at Bennu: Overcoming challenges to collect a sample of the early Solar System. In Sample Return Missions, ed. Longobardo, A. (Elsevier), pp. 163–194.

Lauretta, D.S., et al., (2022). Spacecraft sample collection and subsurface excavation of asteroid (101955) Bennu. Science, eabm1018. https://doi.org/10.1126/science.abm1018

Mario, C.E., Miller, C.J., Norman, et al., 2022. Ground Testing of Digital Terrain Models to Prepare for OSIRIS-REx Autonomous Vision Navigation Using Natural Feature Tracking. The Planetary Science Journal 3, 104. https://doi.org/10.3847/PSJ/ac5182

Mukai, T., Araki, H., Mizuno, T. et al., 2002. Detection of mass, shape and surface roughness of target asteroid of MUSES-C by LIDAR. Adv. Space Res. 29, 1231–1235

Murchie, S., Robinson, M., Domingue, D., Li, H., Prockter, L., Hawkins, S.E., Owen, W., Clark, B., Izenberg, N., 2002. Inflight Calibration of the NEAR Multispectral Imager. II. Results from Eros Approach and Orbit. Icarus 155, 229–243. https://doi.org/10.1006/icar.2001.6746

NAIF, 2007, https://naif.jpl.nasa.gov/pub/naif/generic_kernels/stars/tycho2.xdb.Z

Norman, C.D., Miller, C.J., Olds, R.D. et al., 2022. Autonomous Navigation Performance Using Natural Feature Tracking during the OSIRIS-REx Touch-and-Go Sample Collection Event. The Planetary Science Journal 3, 101. https://doi.org/10.3847/PSJ/ac5183

Olds, R.D., Miller, C.J., Norman, C.D. et al., 2022. The Use of Digital Terrain Models for Natural Feature Tracking at Asteroid Bennu. The Planetary Science Journal 3, 100. https://doi.org/10.3847/PSJ/ac5184

Owen W., 2011. Methods of Optical Navigation, AAS/AIAA Space Flight Mechanics Meeting, American Astronautical Soc. Paper 2011-215.

Palmer, E.E., Gaskell, R., Daly, M.G., Barnouin, O.S., Adam, C.D., Lauretta, D.S., 2022. Practical Stereophotoclinometry for Modeling Shape and Topography on Planetary Missions. The Planetary Science Journal 3, 102. https://doi.org/10.3847/PSJ/ac460f

Park, R.S. and Buccino, D.R., Ceres SPC Shape Model Dataset V1.0. DAWN-A-FC2-5-CERESSHAPESPC-V1.0. NASA Planetary Data System, 2018.

Perry ME, Neumann GA, Phillips RJ, et al (2015) The low-degree shape of Mercury. Geophys Res Lett 42:6951–6958. doi: 10.1002/2015GL065101

Rizk, B. et al. (2018). OCAMS: The OSIRIS-REx Camera Suite. Space Sci. Rev. 214, 26.

Seabrook, J.A., Daly, M., Barnouin, O.S. et al. et al. (2019). Global shape modeling using the OSIRIS-REx scanning laser altimeter. Planet. Space Sci. 177, 104688.

Seabrook, J.A., Daly, M., Barnouin, O.S. et al. (2022). Building a high-resolution digital terrain model of Bennu from laser altimetry data. Planet Sci. J., in revision (this focus issue).

Watanabe S, Hirabayashi M, Hirata N, et al (2019) Hayabusa2 arrives at the carbonaceous asteroid 162173 Ryugu—A spinning top–shaped rubble pile. Science 364:268–272. doi: 10.1126/science.aav8032

Weirich, J., Palmer, E.E., Daly, M.G., et al. (2022). Quality Assessment of Stereophotoclinometry as a Shape Modeling Method Using a Synthetic Asteroid. The Planetary Science Journal 3, 103. https://doi.org/10.3847/PSJ/ac46d2

Weirich JR, Palmer EE, Domingue DL (2019) Digital Terrain Models of Mathilde and the Moon. Lunar and Planetary Science Conference 50, #2681.

Wibben, D. R. et al. (2022) 45th Annual AAS Guidance, Navigation and Control Conference, Breckenridge, CO, paper AAS 22-184